

# Ultrathin nanocapacitor assembled via atomic layer deposition

Javier Alonso Lopez Medina<sup>1,\*</sup> , J Ricardo Mejía-Salazar<sup>2</sup> , William O F Carvalho<sup>3</sup> , Cesar Lopez Mercado<sup>4</sup> , N Nedev<sup>5</sup> , Faustino Reyes Gómez<sup>2</sup> , Osvaldo N Oliveira Jr<sup>3</sup>, M H Farias<sup>6</sup> and Hugo Tiznado<sup>4,\*</sup> 

<sup>1</sup> CONAHCYT—IxM—Centro de Nanociencias y Nanotecnología, Universidad Nacional Autónoma de México, Ensenada C.P. 22800, Mexico

<sup>2</sup> National Institute of Telecommunications (Inatel), Santa Rita do Sapucaí C.P. 37536-001, Brazil

<sup>3</sup> Sao Carlos Institute of Physics, University of Sao Paulo, Sao Carlos C.P. 369, 13560-970, Brazil

<sup>4</sup> Universidad Autónoma de Baja California, FIAD, Ensenada C.P. 22860, Mexico

<sup>5</sup> Universidad Autónoma de Baja California, Instituto de Ingeniería, Mexicali C.P. 21280, Mexico

<sup>6</sup> Centro de Nanociencias y Nanotecnología, Universidad Nacional Autónoma de México, Ensenada C.P. 22800, Mexico

E-mail: [javierlo21@ens.cnyn.unam.mx](mailto:javierlo21@ens.cnyn.unam.mx) and [tiznado@ens.cnyn.unam.mx](mailto:tiznado@ens.cnyn.unam.mx)

Received 11 June 2024, revised 4 September 2024

Accepted for publication 25 September 2024

Published 8 October 2024



## Abstract

We fabricated ultrathin metal–oxide–semiconductor (MOS) nanocapacitors using atomic layer deposition. The capacitors consist of a bilayer of  $\text{Al}_2\text{O}_3$  and  $\text{Y}_2\text{O}_3$  with a total thickness of  $\sim 10$  nm, deposited on silicon substrate. The presence of the two materials, each slab being  $\sim 5$  nm thick and uniform over a large area, was confirmed with transmission electron microscopy and x-ray photoelectron spectroscopy. The capacitance in accumulation varied from 1.6 nF (at 1 MHz) to  $\sim 2.8$  nF (at 10 kHz), which is one to two orders of magnitude higher than other nanocapacitors. This high capacitance is attributed to the synergy between the dielectric properties of ultrathin  $\text{Al}_2\text{O}_3$  and  $\text{Y}_2\text{O}_3$  layers. The electrical properties of the nanocapacitor are stable within a wide range of temperatures, from 25 °C to 150 °C, as indicated by capacitance–voltage ( $C$ – $V$ ). Since the thickness-to-area ratio is negligible, the nanocapacitor could be simulated as a single parallel plate capacitor in COMSOL Multiphysics, with good agreement between experimental and simulation data. As a proof-of-concept we simulated a MOS field effect transistor device with the nanocapacitor gate dielectric, whose drain current is sufficiently high for micro and nanoelectronics integrated circuits, including for applications in sensing.

**Keywords:** nanocapacitor, dielectric materials, atomic layer deposition, ultrathin films

\* Authors to whom any correspondence should be addressed.



Original content from this work may be used under the terms of the [Creative Commons Attribution 4.0 licence](https://creativecommons.org/licenses/by/4.0/). Any further distribution of this work must maintain attribution to the author (s) and the title of the work, journal citation and DOI.

## 1. Introduction

Device integration in small areas is crucial for the microelectronics and optoelectronics industry, which requires miniaturization for packing a large number of components [1, 2]. Small-scale components have been developed using new materials and innovative manufacturing processes [3, 4]. Metal–oxide–semiconductor (MOS) structures made from thin films [5, 6] are the basis for digital circuits within complementary MOS (CMOS) technology and field effect transistor (MOSFET) devices [7], with huge economic impact in integrated circuits when produced at the nanoscale [8]. However, MOS structures normally made with silicon oxide ( $\text{SiO}_2$ ) as dielectric material have reached their limit of miniaturization. There is now a search for high  $\kappa$  dielectric materials to replace  $\text{SiO}_2$  [9, 10], which will in turn allow for higher miniaturization levels. Small nanocapacitors are essential for highly-integrated printed circuit boards and high-density dynamic random-access memories [11–14] used in ultrahigh-speed flash-like memories. Large capacitances in small areas/volumes have been obtained through approaches such as layer-by-layer assembly [15, 16],  $\text{MoS}_2$ – $\text{HfO}_2$ – $\text{SrTiO}_3$  trilayer nanostructures [17], and using ferroelectric copolymer ultrathin films [18]. These accomplishments were made with relatively large thicknesses, typically  $\geq 20$  nm. Approaches to produce integrated sub-20 nm nanostructures with large capacitances are necessary, since present technologies for CMOS [19, 20] and MOSFET devices [21] only employ thick insulating layers.

There is a need for precise control of layer thickness and uniformity as device dimensions shrink with the use of ultrathin films. Furthermore, such devices are expected to be integrated into CMOS-compatible platforms, which has motivated the growing use of atomic layer deposition (ALD) technique for ultrathin film fabrication. In ALD film thickness is controlled at the atomic level, thus enabling homogeneous and reproducible film growth. This minimizes the number of defects in the films, which is essential for microelectronics and nanophotonics. Furthermore, with ALD one may produce uniform, conformable layers on a variety of substrates and at low temperature. As an example, relevant to our study, ALD has been used to fabricate dielectric bilayers for MOS structures by alternating short pulses of precursor A (organometallic precursor) and precursor B (reactant precursor) in an AB sequence until the desired bilayer thickness is achieved on a silicon substrate.

To obtain thin insulating layers, we propose the combination of  $\text{Al}_2\text{O}_3$  and  $\text{Y}_2\text{O}_3$  in an ultra-thin film. The advantage of using these materials comes from the excellent dielectric properties of  $\text{Y}_2\text{O}_3$ , which has a high optical dielectric constant (between 12 and 20) and high bandgap energy (5.6 eV) [22], while  $\text{Al}_2\text{O}_3$  has an optical dielectric constant between 8 and 10 and bandgap energy around 8 eV [23]. Although MOS structures have been obtained with either  $\text{Y}_2\text{O}_3$  or  $\text{Al}_2\text{O}_3$ , which can be fabricated with radio-frequency magnetron sputtering using ceramic targets of  $\text{Al}_2\text{O}_3$  or  $\text{Y}_2\text{O}_3$ , their combined

properties have not been exploited. In this paper, we report on a nanostructured MOS capacitor with a solid-state dielectric made of an ultrathin bilayer of  $\text{Al}_2\text{O}_3$ – $\text{Y}_2\text{O}_3$ . The main reason for developing this MOS structure is in its possible use for a new generation of micro and nano devices, especially as it can be extended to different applications. The MOS capacitor to be reported here has a total thickness of ca. 10 nm grown on a conventional Si/ $\text{SiO}_2$  substrate [24], with the layers being produced via ALD [25] from organometallic precursors for  $\text{Al}_2\text{O}_3$  and  $\text{Y}_2\text{O}_3$  in gas phase. TMA and  $(\text{MeCp})_3\text{Y}$  were chosen as precursors for Al and Y, respectively, for several reasons. With its high vapor pressure, TMA is an inexpensive and viable option for experimental applications. Its rapid reaction with water facilitates the efficient deposition of aluminum-containing films at low temperatures. Moreover, TMA is a well-established aluminum source in semiconductor fabrication, e.g. for growing thermally stable, insulating  $\text{Al}_2\text{O}_3$  thin films [26].  $(\text{MeCp})_3\text{Y}$  has the highest vapor pressure among organometallic precursors used to obtain  $\text{Y}_2\text{O}_3$  films through CVD, MOCVD, and ALD methods [27]. This high vapor pressure is crucial for achieving reasonable growth rates during ALD. Additionally, when combined with  $\text{H}_2\text{O}$  as an oxygen source,  $(\text{MeCp})_3\text{Y}$  can produce films with lower carbon and hydrogen impurity levels, resulting in better electrical characteristics in ultrathin films. Both precursors are particularly suitable for fabricating MOS nanocapacitors, as they minimize carbon traces at the end of each film deposition. These carbon traces could otherwise negatively affect the electrical behavior and overall performance of devices. The chemical stability and compatibility of TMA and  $(\text{MeCp})_3\text{Y}$  enable the production of high-quality  $\text{Al}_2\text{O}_3$  and yttrium-based bilayer films. The experimental results obtained with the MOS structure are also explained through numerical simulations using the commercial software COMSOL Multiphysics. Of great significance is the capacitance of the order of nF, considerably higher than the values in the literature using other materials.

## 2. Methods

### 2.1. Materials

Prior to deposition, to eliminate traces of contamination from the Si surface, a chemical cleaning process was employed. This involved sonicating the surface in a 1:1 mixture of acetone, isopropanol, ethanol, and methanol for 15 min at 50 °C, followed by rinsing with reagent-grade isopropanol, and finally drying with UHP  $\text{N}_2$  (99.999%), according to the process carried out in previous works [28, 29]. The organometallic sources tris(cyclopentadienyl)yttrium ( $(\text{MeCp})_3\text{Y}$ , 99.9%) and trimethylaluminum (TMA, 98%) were used as chemical precursors, while deionized (DI) water at room temperature served as the oxidizing agent. Both chemical precursors were supplied by Strem Chemicals, with catalog numbers 93–1360 and 39–5050, respectively. To eliminate oxygen traces ultrahigh purity  $\text{N}_2$  was used as a carrier and purging gas during

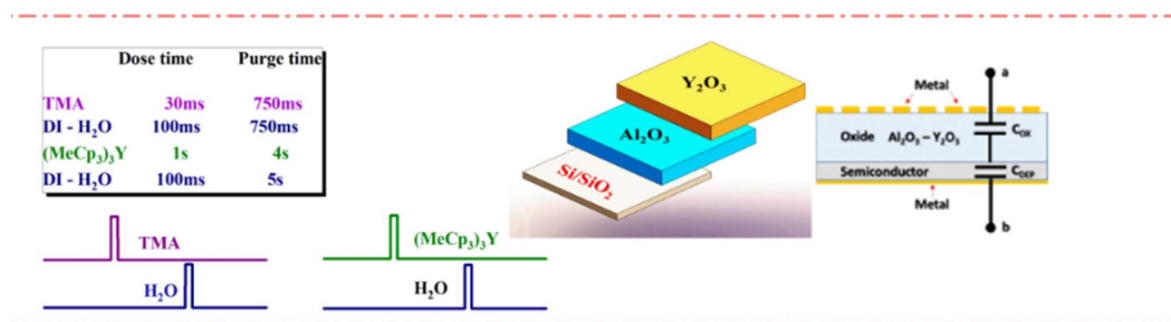


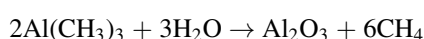
**Figure 1.** Atomic layer deposition scheme for Al<sub>2</sub>O<sub>3</sub>–Y<sub>2</sub>O<sub>3</sub> bilayer fabrication.

the ALD process. This N<sub>2</sub> gas was purified to  $<10^{-6}$  ppm O<sub>2</sub> with an inert gas purifier and an oxygen monitor.

## 2.2. Ultrathin nanocapacitor fabrication

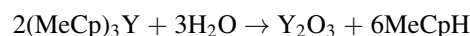
Nanocapacitors were formed by depositing an ultrathin Al<sub>2</sub>O<sub>3</sub>–Y<sub>2</sub>O<sub>3</sub> bilayer on Si (100) p-type SSP (single side polished) using a viscous-flow ALD reactor from Beneq (Espoo, Finland), model TFS 200, at 250 °C deposition temperature in the reactor. The temperature in the canister of (MeCp)<sub>3</sub>Y precursor was maintained at 140 °C while the canister for TMA was kept at room temperature to achieve the necessary vapor pressure. Al<sub>2</sub>O<sub>3</sub>–Y<sub>2</sub>O<sub>3</sub> ultrathin dielectric bilayer films were prepared in two main steps (see figure 1). First, the 5 nm thick Al<sub>2</sub>O<sub>3</sub> layer was deposited on the Si/native SiO<sub>2</sub> surface using 42 cycles of TMA–H<sub>2</sub>O (growing rate 1.2 Å/cycle), where each cycle consists of 30 ms TMA dose/750 ms N<sub>2</sub> purge/100 ms DI water dose/750 ms N<sub>2</sub> purge. Then, a 5 nm thick Y<sub>2</sub>O<sub>3</sub> layer was deposited on Al<sub>2</sub>O<sub>3</sub> using 44 cycles of (MeCp)<sub>3</sub>Y–H<sub>2</sub>O, with a growing rate of 1.13 Å/cycle, each cycle consisting of 1 s (MeCp)<sub>3</sub>Y dose/4 s N<sub>2</sub> purge/100 ms DI water dose/5 s N<sub>2</sub> purge. The top and bottom Au electrodes were deposited by thermal evaporation at room temperature using a JEOL JEE-400 Vacuum Thermal Evaporator. In this process, a gold wire with a diameter of 0.20 mm was heated on a tungsten filament under an electrical current of 13 A for 10 min, with a base pressure of  $1 \times 10^{-3}$  Pa. A stainless-steel template with holes approximately 0.4 mm in radius was used to fabricate the gold electrodes, resulting in a top electrode area of approximately  $4.53 \times 10^{-7}$  m<sup>2</sup>, while for the bottom electrode, a gold film was evaporated on the rear surface of the silicon substrate [30–33].

The reaction mechanism for the Al<sub>2</sub>O<sub>3</sub> and Y<sub>2</sub>O<sub>3</sub> films formation from organometallic precursors and water has been reported by different authors. The chemical reaction for TMA and water can be expressed as follows:



In this reaction, TMA reacts with water to produce Al<sub>2</sub>O<sub>3</sub> and CH<sub>4</sub> as subproducts. In this case, two molecules of TMA react with three molecules of water to produce aluminum oxide as the solid film, and six methane (CH<sub>4</sub>) molecules are

released as a gas phase. In this same sense, the general reaction for the Y<sub>2</sub>O<sub>3</sub> film formation from (MeCp)<sub>3</sub>Y and water can be expressed as follows:



In this case, two molecules of (MeCp)<sub>3</sub>Y react with three molecules of water, resulting in the yttrium oxide Y<sub>2</sub>O<sub>3</sub> film and six molecules of methylcyclopentadiene (MeCpH) are released as gas phase subproducts.

## 2.3. MOS nanocapacitor characterization

Nanocapacitors obtained with the ALD technique have uniform thickness across the whole substrate, as confirmed with scanning transmission electron microscopy (STEM), spectroscopic ellipsometry (SE), atomic force microscopy measurements and x-ray photoelectron spectroscopy (XPS). Capacitance values ranging from 1.6 nF to 2.8 nF, for frequencies between 1 MHz and 10 kHz, were measured on the nanocapacitors in accumulation. The high-temperature stability of capacitance values was corroborated by measurements at different working temperatures, from 25 °C to 150 °C, and radio frequencies from 10 kHz to 1 MHz. The thickness and optical properties of bilayer films were studied through SE at room temperature using a variable angle spectroscopic ellipsometry (VASE), by J.A. Woollam Co. Measurements were obtained at 45°, 55°, 65° and 75° incidence angle in a spectral range from 240 nm to 1100 nm.

Transmission electron microscopy (TEM) was used to obtain the bilayer thickness. The sample for TEM analysis was prepared using a JEOL JIB-4500 scanning electron microscope/focused ion beam (FIB) system. To avoid film damage during sample preparation, gold and carbon layers were evaporated on top of the film before FIB processing. The sample thickness was reduced to a few nm for allowing electrons to pass through the sample. TEM micrographs, in cross-sectional mode, were obtained in a JEOL JEM-2100F (STEM). A JEOL JEE-400 Vacuum Thermal Evaporator was utilized for depositing gold electrical contacts on both sides of the samples (top and bottom). The presence of the composing materials was confirmed through XPS, which probes surfaces to a depth of 10 nm. The XPS measurements were taken with a

**Table 1.** Experimentally measured dielectric constant at radio wave frequencies of 10 kHz and 1 MHz for different temperatures.

Temperature (°C)	Dielectric constant	
	10 kHz	1 MHz
25	8.4	4.7
90	7.7	4.7
150	7.6	4.8

system from SPECS, equipped with a hemispherical electron analyzer, PHOIBOS 150 WAL, and monochromatic x-ray source, XRC-1000, with Al K $\alpha$  at 200 W.

The electrical characterization of the MOS capacitor was performed using capacitance/conductance–voltage ( $C/G$ – $V$ ) and current–voltage ( $I$ – $V$ ) measurements at different temperatures with a Keithley 4200A-SCS Parameter Analyzer, supplied by Keithley Instruments (Cleveland, Ohio, USA). The sample was positioned on a SemiProbe Lab station, provided by SemiProbe (Winooski, Vermont, USA). This station features a magnetic stage base allowing fine displacements along the  $x$ ,  $y$ , and  $z$  axes with micrometer screws. It has four micro-manipulators, and a completed optical system for sample visualization, including an optical microscope with a CCD camera connected to a laptop. To minimize electrical noise from the surroundings, the SemiProbe Lab station was enclosed within a Faraday cage. The  $C/G$ – $V$  loops were measured using a 25 mV a.c. signal with radio frequencies of 10 kHz and 1 MHz. The  $C/G$ – $V$  dependences were measured by applying a d.c. voltage bias (back and forth) between +2.5 V and –2.5 V at a sweep rate of 0.025 V s $^{-1}$ .  $I$ – $V$  measurements were obtained via voltage scanning from +3.5 V to –3.5 V to avoid dielectric breakdown ( $V_{br} > 4$  V). To heat the samples, we used a custom-made setup consisting of a hotplate connected to a power supply and a temperature controller with a Nichrome thermocouple. This arrangement enables us to study the effects of temperature on the MOS nanocapacitors.

#### 2.4. Numerical simulations

The semiconductor module within the COMSOL Multiphysics software was used to apply a finite element methodology to simulate MOSCAP and MOSFET structures. These simulations could theoretically investigate the behavior of the proposed platforms. Specifically, the entire system comprising the SiO $_2$  and Al $_2$ O $_3$ –Y $_2$ O $_3$  bilayers was modeled as an effective medium with a height of 12 nm. Dielectric constants crucial to the simulations were obtained from the COMSOL library for Si and SiO $_2$  layers, and from table 1 for the Al $_2$ O $_3$ –Y $_2$ O $_3$  bilayer. The electrical responses of the systems were computed using the small-signal analysis approach. To capture the intricate dynamics of trap charges and carrier processes, models for uniform doping and Shockley–Read–Hall recombination were integrated. These models simulated the trapping and releasing of carriers by the traps. To ensure accuracy near the critical interfaces, a user-controlled mesh refinement strategy was implemented, particularly under the oxide–Al $_2$ O $_3$ –Y $_2$ O $_3$ /silicon interface. This ensured that

the mesh resolution was optimized for obtaining precise simulations.

### 3. Results and discussion

Figure 2(a) shows a schematic representation of the device comprising an Al $_2$ O $_3$ –Y $_2$ O $_3$  bilayer grown on a Si/native SiO $_2$  substrate, with Au layers deposited as top and back electrodes. The equivalent circuit model to explain the total capacitance of this MOS structure at high frequencies (at and above 1 MHz) is shown in figure 2(b). The high-frequency capacitance ( $C_{HF}$ ) is related to the oxide capacitance ( $C_{ox}$ ) and the capacitance of the Si depletion region ( $C_{Dep}$ ) is defined through equation (1) [34, 35]. Figures 2(c) and (d) show optical images of a nano-capacitor fabricated via thermal ALD method,

$$\frac{1}{C_{HF}} = \frac{1}{C_{OX}} + \frac{1}{C_{Dep}}. \quad (1)$$

The bilayer thickness was determined through SE by fitting the results using the Cauchy dispersion relation, which models the dispersion in transparent materials [36–38]. The bilayer thickness was 11.5 nm with a mean squared error (MSE) of 6.26, indicating high reliability for the model [38]. Figures 3 (a) and (b) illustrate the VASE data juxtaposed with model data for an Al $_2$ O $_3$ –Y $_2$ O $_3$  bilayer fabricated via ALD. Employing the Cauchy model for fitting, the Al $_2$ O $_3$ –Y $_2$ O $_3$  bilayer was treated as a consolidated entity comprising two distinct materials atop a silicon substrate, serving both as a semiconductor and mechanical support. The ellipsometric model was configured as follows: a bilayer setup comprising an infinite Si (100) substrate ( $\sim 300 \mu\text{m}$ ), a native SiO $_2$  layer (2.7 nm thick), and alternating layers of Al $_2$ O $_3$  and Y $_2$ O $_3$ , as depicted in figure 2. Before the fitting process, physical parameters such as thicknesses and optical constants for the silicon substrate and native SiO $_2$  were incorporated into the model without adjustment. Subsequently, the Cauchy model was fitted using the complete EASE $^{\circ}$  software to obtain the thickness and dispersion profiles for  $n(\lambda)$ . During this fitting procedure, Cauchy parameters were adjusted accordingly. The outcomes of the fitting process in figures 3(a) and (b) confirm the agreement between the experimental data and the model-generated data for the ellipsometric angles  $\Psi$  and  $\Delta$ . The MSE = 6.26 derived from this fitting process validates the effectiveness of the procedure for the sample.

The bilayer thickness was confirmed by cross-sectional TEM images such as the one in figure 4(a). The interface between substrate and deposited dielectric layers can be easily distinguished, as the light tone fringe corresponds to Al $_2$ O $_3$  (5.3 nm thick) and the darker fringe is associated with Y $_2$ O $_3$  layer (5.8 nm thick). The bilayer thickness is 11.1 nm from this TEM image, in good agreement with the SE measurements. The high uniformity of the layers across the entire film and the well-defined interfaces indicates the high accuracy obtained with ALD. Indeed, the low temperature of deposition in the ALD reactor avoided nucleation, grain growth in the system, and crystallization of Al $_2$ O $_3$  and Y $_2$ O $_3$  layers. The latter is well established in the literature for the growth of oxide materials



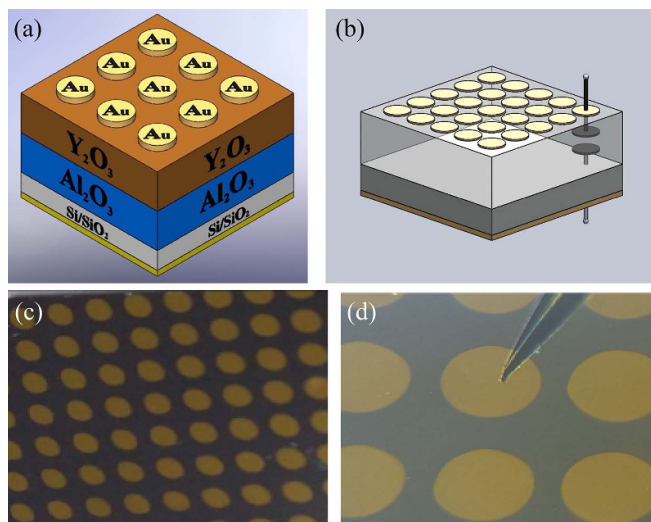


**Figure 2.** (a) Cross-section of  $\text{Al}_2\text{O}_3$ – $\text{Y}_2\text{O}_3$  ultrathin MOS nanocapacitors on  $\text{Si}/\text{SiO}_2$ . (b) Schematic view of the dielectric effective nanocapacitance. (c) and (d) Optical images of the nanocapacitor structure fabricated with the ALD method.

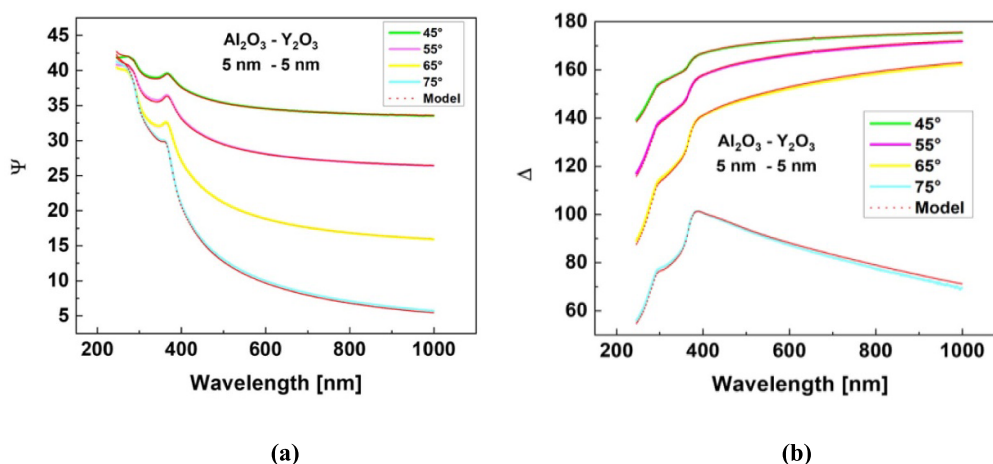


**Figure 3.** Variable angle spectroscopic ellipsometry (VASE) and model data for a bilayer of  $\text{Al}_2\text{O}_3$ – $\text{Y}_2\text{O}_3$  (a)  $\Psi$  and (b)  $\Delta$  ellipsometry angles.

[39–41]; there is also supporting evidence from TEM images in figure 4. The lattice parameter of the cubic crystalline  $\text{Y}_2\text{O}_3$  structure is around 1.1 nm [42], while  $\text{Al}_2\text{O}_3$  material may crystallize in the alpha, beta, or gamma phases with lattice parameters varying from 0.5 nm to 1.3 nm for each side [43]. Hence, considering that each individual homogeneous layer has an average thickness as small as 5 nm, the system cannot be considered crystalline.

Figure 4(b) shows TEM images at 5 and 10 nm scale, providing detailed insights into the microstructure of the bilayer. The  $\text{Al}_2\text{O}_3$  layer remains amorphous, which is consistent with its inability to crystallize at the relatively low deposition temperature during the synthesis process. This lack of crystallization is typical for  $\text{Al}_2\text{O}_3$  under such conditions, resulting in a disordered atomic structure. In contrast, the  $\text{Y}_2\text{O}_3$  layer exhibits crystalline regions, indicating the formation of a crystalline phase within the bilayer. The presence of these crystals indicates that  $\text{Y}_2\text{O}_3$  undergoes partial crystallization during deposition, even at the same temperature where  $\text{Al}_2\text{O}_3$

remains amorphous. This crystalline phase is likely associated with a face-centered cubic structure, which is known to form at growth temperatures around 250 °C. This observation is consistent with previous studies of  $\text{Y}_2\text{O}_3$  films grown by ALD at similar temperatures. The TEM images illustrate the distinct amorphous and crystalline phase behaviors of the two materials within the bilayer.

XPS measurements were taken to obtain information about the chemical elements Y, Al, and O present in the ultrathin  $\text{Al}_2\text{O}_3$ – $\text{Y}_2\text{O}_3$  bilayer with 10 nm thickness along with the information about chemical bonds. High resolution-spectra were analyzed for Y3d, Al2p, and O1s; the different spectra were deconvolved and fitted using CasaXPS software, considering the C 1s peak at 284.5 eV as binding-energy calibration. The high-resolution XPS spectra for bilayer are shown in figures 5(a)–(c). The main components found at different BE positions in the bilayer were Y3d, Al2p, and O1s. For the Y3d component spectra in figure 5(a), two intense peaks with a binding energy appear at 156.25 and 158.11 eV for  $\text{Y3d}_{5/2}$

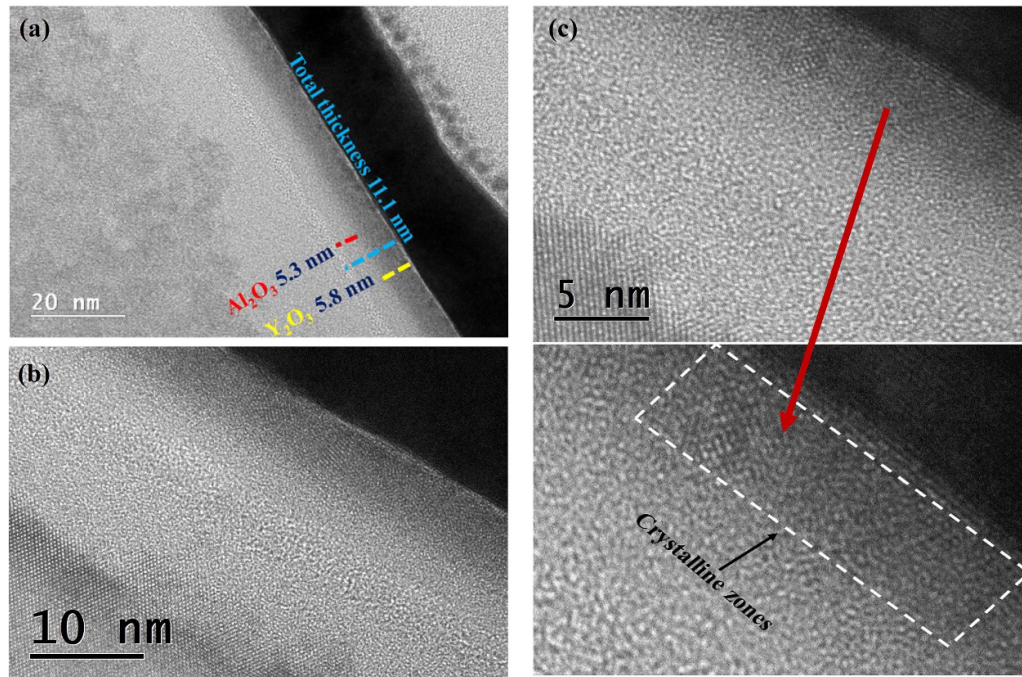


**Figure 4.** (a) Cross-sectional TEM image of the  $\text{Al}_2\text{O}_3$ – $\text{Y}_2\text{O}_3$  bilayer on Si/SiO<sub>2</sub> substrate. (b) and (c) TEM images at 10 and 5 nm scale to visualize the amorphous and crystalline phase present in the bilayer.

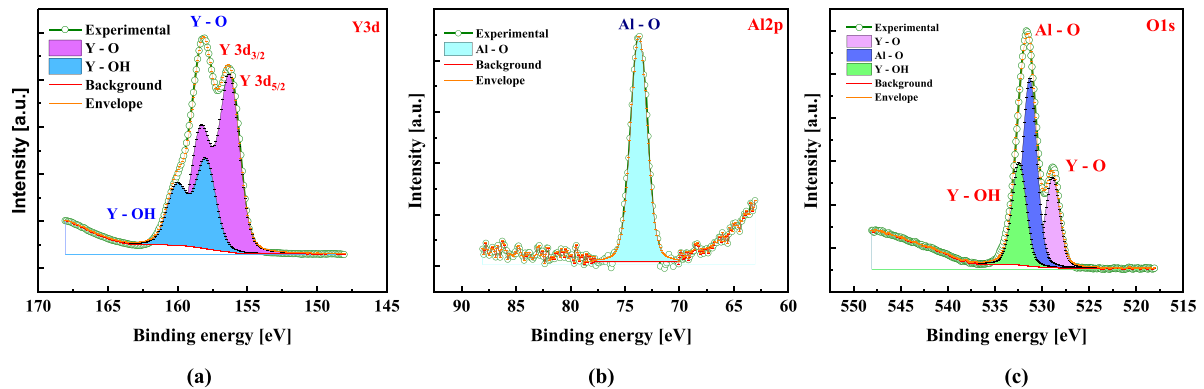


**Figure 5.** High resolution XPS spectra of (a) Y3d; (b) Al2p (c) O 1s for  $\text{Al}_2\text{O}_3$ – $\text{Y}_2\text{O}_3$  bilayer film.

and  $3d_{3/2}$  that corresponds to pure Y–O bonding in the  $\text{Y}_2\text{O}_3$  layer, which is consistent with reports for  $\text{Y}_2\text{O}_3$  films prepared by ALD method. Besides, two low-intensity peaks at 157.97 and 159.88 eV appear and are associated with Y–OH bonding; this Y–OH species could be related to the reactions in the thermal ALD synthesis water-assisted as a reactant precursor with organometallic precursor used for yttrium. Figure 5(b) with the Al2p spectra shows an intense peak with binding energy at 73.81 eV assigned to Al–O bonding in the  $\text{Al}_2\text{O}_3$  layer. Finally, in the O1s spectra in figure 5(c), there are two peaks at different intensities; the more intense peak appears at 531.61 eV associated with the Al–O bonds, the lower peak at 528.68 eV related to Y–O bonds. There is also one peak at 532.50 eV (indicating the Y–OH bonds presence) associated with the water species due to the ALD process in fabricating the  $\text{Al}_2\text{O}_3$ – $\text{Y}_2\text{O}_3$  ultrathin nanocapacitor [30–33].

Figure 6 shows a comparison of the experimental and simulated capacitance vs voltage ( $C$ – $V$ ) curves at three temperatures  $T = 25^\circ\text{C}$ ,  $T = 90^\circ\text{C}$ , and  $T = 150^\circ\text{C}$ , and two radio wave frequencies, 10 kHz and 1 MHz. At both frequencies the slope of the experimental  $C$ – $V$  curves in the region between accumulation and inversion is smaller than that of the simulated dependencies. The observed stretch out of the experimental curves is due to interface states, which affect the total measured capacitance in two ways: first, by the capacitance of the Si depletion layer ( $C_{\text{Dep}}$ ) and second, by the interface state capacitance ( $C_{\text{it}}$ ). At 1 MHz the interface states change their charge state only with the slowly varying bias, modifying the depletion region thickness and thus the depletion capacitance  $C_{\text{Dep}}$  and the total capacitance. However, at low frequency the interface defects can respond to the a.c. test signal contributing to the total capacitance by  $C_{\text{it}}$ , which is in parallel with

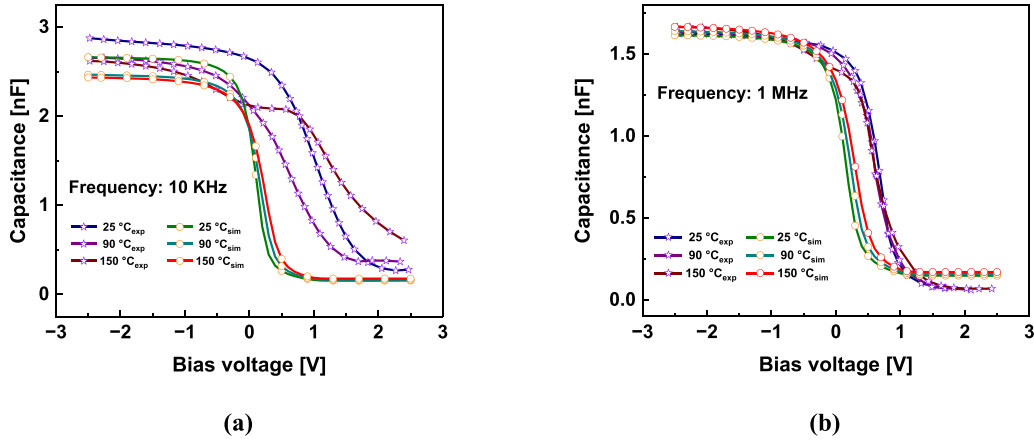


**Figure 6.** Experimental (open-star symbols) and numerical (open circles) results of capacitance vs voltage ( $C-V$ ) in the studied  $\text{Al}_2\text{O}_3$ - $\text{Y}_2\text{O}_3$  bilayer for  $T = 25^\circ\text{C}$ ,  $T = 90^\circ\text{C}$ , and  $T = 150^\circ\text{C}$  for frequencies of (a) 10 kHz and (b) 1 MHz.

$C_{\text{Dep}}$  [35]. An additional stretch out of the dependencies at 10 kHz was observed at higher temperatures, which may be due to a higher generation rate of electron-hole pairs, resulting in higher values of the interface state capacitance. The experimental curves in figures 6(a) and (b) are shifted towards more positive voltages compared to the simulated ones owing to a negative charge in the dielectric layer. This kind of behavior has been reported for  $\text{Al}_2\text{O}_3$  layers used for surface passivation in solar cells [44].

The total capacitance of a MOS capacitor is determined by the  $\text{Al}_2\text{O}_3$ - $\text{Y}_2\text{O}_3$  bilayer thickness, electrode area and the dielectric constant of the insulating materials. Since the ratio between the electrode area ( $\phi = 4.53 \times 10^{-7} \text{ m}^2$ ) and the dielectric  $\text{Al}_2\text{O}_3$ - $\text{Y}_2\text{O}_3$  bilayer thickness ( $l = 10 \text{ nm}$ ) is very large  $\phi/l = 0.45 \times 10^2 \text{ m}$ , the system can be approximated by a parallel plate capacitor, filled with the bilayer dielectric material  $\text{Al}_2\text{O}_3$ - $\text{Y}_2\text{O}_3$ . This approximation is further validated by the strong correlation between the simulated results (represented by solid lines with open circles) and the experimental results (represented by solid lines with open stars) at operating frequencies of 10 kHz and 1 MHz, as illustrated in figures 6(a) and (b), respectively. In addition, from capacitance-voltage results for the  $\text{Al}_2\text{O}_3$ - $\text{Y}_2\text{O}_3$  bilayer, we determined the effective dielectric constant  $\varepsilon$  for two different frequencies (see table 1). The dielectric constant at 10 kHz ranges from 8.4 at room temperature to 7.6 at  $150^\circ\text{C}$ . In contrast, at a higher frequency of 1 MHz, the dielectric constant remains relatively stable (4.7–4.8) across the range of temperatures studied. The reduced capacitance at 1 MHz in accumulation are attributed to the impact of series resistance, primarily stemming from the quasi-neutral bulk silicon's resistance between the back contact and the depletion layer edge beneath the gate [34].

The primary error in capacitance due to series resistance manifests in accumulation, thereby influencing the  $\varepsilon$  value derived from high-frequency  $C-V$  measurements. To mitigate the effect of series resistance, low-frequency measurements are recommended, as they reduce its impact [34]. Consequently, one may assume that the permittivity determined at 10 kHz is more accurate. It is worth mentioning that

the dielectric constant of the bilayer is lower than for a single-layer capacitor with  $\text{Al}_2\text{O}_3$  and  $\text{Y}_2\text{O}_3$ . One possible explanation for this observation is the presence of transition regions within the  $\text{Al}_2\text{O}_3$  and  $\text{Y}_2\text{O}_3$  layers, near the  $\text{Si}/\text{Al}_2\text{O}_3$  and  $\text{Al}_2\text{O}_3/\text{Y}_2\text{O}_3$  interfaces, respectively. These transition regions possess dielectric properties distinct from the bulk  $\text{Al}_2\text{O}_3$  and  $\text{Y}_2\text{O}_3$  materials. Given the thinness of both layers in the bilayer, the influence of these transition regions cannot be ignored, which would explain the decreased effective dielectric constant.

The leakage current in the bias voltage range of interest was determined with current-voltage ( $I-V$ ) measurements in figure 7. This leakage current is one of the most important parameters in determining the performance of a MOS capacitor. It depends on such characteristics as stoichiometry of the dielectric [45], microstructural properties [46], thickness [47], types of contacts [48], and quality of the interfaces [49]. At low electric fields, with bias voltage in the range of  $(-1.5, 1.5 \text{ V})$ , the current was close to  $10^{-8} \text{ A}$  ( $10^{-10}/4.53 \times 10^{-3} = 2.2 \times 10^{-8} \text{ A cm}^{-2}$ , current density  $\sim 2 \times 10^{-8} \text{ A cm}^{-2}$ ). At higher electric field ( $E$ ) the current increased more than one order of magnitude to  $\sim 3 \times 10^{-9} \text{ A}$  (current density of  $6.6 \times 10^{-7} \text{ A cm}^{-2}$ ) at  $E = 3.1 \text{ MV cm}^{-1}$  ( $\pm 3.5 \text{ V}$ ). These small values for the leakage current indicate good insulating properties of the  $\text{Al}_2\text{O}_3$ - $\text{Y}_2\text{O}_3$  bilayer deposited by ALD.

To demonstrate the applicability of our concept for integrated nanoelectronic circuits, we simulated a MOSFET device, depicted in figure 8(a), which uses a nanocapacitor as obtained experimentally here as the gate dielectric film. The measured parameters for the bilayer dielectric were used in the simulation. The corresponding electronic parameters, shown in figures 8(b)–(d), were found competitive with recent results for ultrathin nanocapacitors with  $\text{MoS}_2/\text{CaF}_2$  [50] and h-BN (hexagonal boron nitride) [51] fabricated using more complex techniques. Moreover, the temperature stability of the MOSFET was proven by calculations for temperatures of  $25^\circ\text{C}$ ,  $90^\circ\text{C}$ , and  $125^\circ\text{C}$  at both 10 kHz and 1 MHz working frequencies.

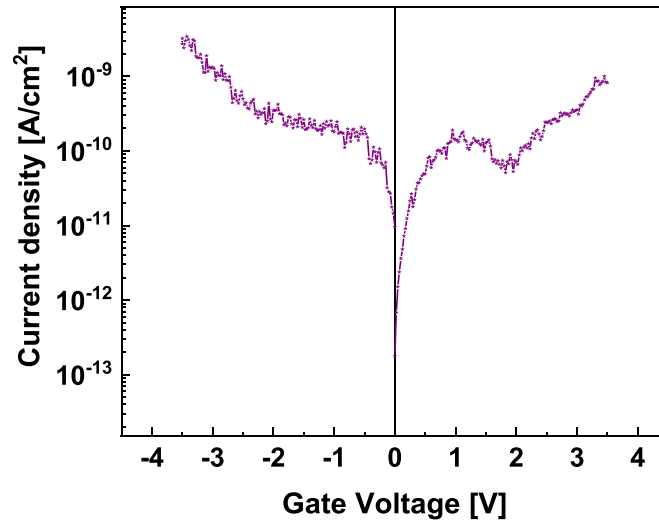


**Figure 7.**  $I$ – $V$  characteristic of the MOS structure, consisting of an  $\text{Al}_2\text{O}_3$ – $\text{Y}_2\text{O}_3$  bilayer with a total thickness of 10 nm.

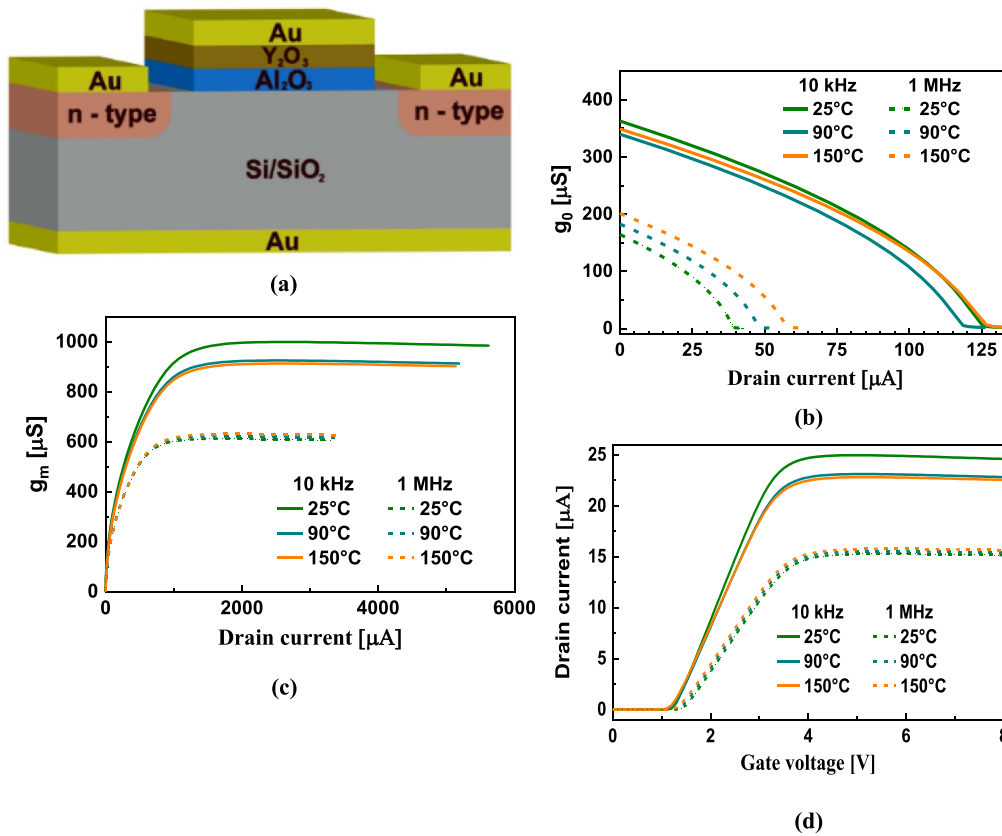


**Figure 8.** (a) Schematic representation of the simulated device. Numerical results for (b) output conductance, (c) transconductance, and (d) drain current of a simulated field-effect transistor. Simulations were carried out for different temperatures at 10 kHz and 1 MHz to illustrate the temperature stability of the proposed device.

#### 4. Conclusions

Using the ALD method, we fabricated an ultrathin MOS nanocapacitor with capacitances from 1.6 nF to 2.8 nF with a thickness as low as 10 nm. Our concept comprises a high quality and uniform ultrathin  $\text{Al}_2\text{O}_3$ – $\text{Y}_2\text{O}_3$  bilayer, as corroborated with spectroscopy, physicochemical and morphological

studies. In particular, each building dielectric layer in the system has a thickness of  $\sim 5$  nm. Comparative measurements of the capacitance, carried out at 25 °C, 90 °C and 150 °C, indicate high temperature stability. Numerical simulation results using COMSOL Multiphysics were found to be in good agreement with experimental data. The high integrability and electrical parameters of these nanocapacitors can be used in



different applications such as point-of-care biosensing devices [52]. Furthermore, the applicability in high drain current MOSFET devices was demonstrated numerically.

### Data availability statement

All data that support the findings of this study are included within the article (and any supplementary files).

### Acknowledgments

The National Autonomous University of Mexico will fund the open-access publication of this article due to an existing agreement with the *IOP Nanotechnology Journal*. Articles are eligible for article processing charge (APC) coverage if the corresponding author has a UNAM affiliation and uses an email address ending in @...unam.mx. This work was partially supported by CONAHCYT—Basic Science Projects 2017–2018 A1-S-21323 and A1-S-21084, DGAPA-UNAM, through research projects: PAPIIT IN110424, IG101124. This work also was partially supported by RNP, with resources from , Grant No. 01245.020548/2021- 07, under the Brazil 6G project of the Radiocommunication Reference Center (Centro de Referência em Radiocomunicações—CRR) of the National Institute of Telecommunications (Instituto Nacional de Telecomunicações—Inatel), Brazil, and by the Project XGM-AFCCT-2024-3-1-1 supported by xGMobile—EMBRAPII-Inatel Competence Center on 5G and 6G Networks, with financial resources from Ministério da Ciência, Tecnologia e Inovações (MCTI) Grant Number 052/2023, signed with EMBRAPII. We also acknowledge financial support from the Brazilian agencies National Council for Scientific and Technological Development-CNPq (314671/2021-8), Fundação de Amparo à Pesquisa do Estado de São Paulo (FAPESP) (2018/22214-6, 2023/08999-9), FAPEMIG (APQ-05305-23) and CAPES (Finance Code—001). Authors would like to thank valuable technical support by David Dominguez, Eduardo Murillo, Israel Gradilla, Francisco Ruiz and Jaime Mendoza.

### Conflict of interest

The authors declare that they have no known competing financial interests or personal relationships that could have appeared to influence the work reported in this paper.


### Author contribution list

The contribution made in the manuscript by each author are presented below.

**Dr Javier Alonso López Medina:** Investigation, Methodology, Writing—original draft, Visualization, Funding acquisition, Project administration. **Dr Jorge Ricardo Mejía Salazar:** Investigation, Methodology, Visualization, Writing—original draft. **Dr William O F Carvalho:** Investigation, Methodology, Writing—original draft. **Dr**

**Cesar Lopez Mercado:** Methodology, Visualization. **Dr Faustino Reyes Gómez:** Methodology, Investigation, Visualization, Writing—review & editing. **Dr Osvaldo N. Oliveira Jr.:** Visualization, Writing—review & editing, Supervision. **Dr Nicola Nedev:** Investigation, Visualization, Writing—review & editing, Supervision. **Dr Mario Humberto Farías Sánchez:** Investigation, Writing—original draft, Visualization, Funding acquisition, Project administration. **Dr Hugo Tiznado:** Investigation, Writing—review & editing, Visualization, Funding acquisition, Project administration.

### ORCID iDs

Javier Alonso Lopez Medina  <https://orcid.org/0009-0006-2146-5511>

J Ricardo Mejía-Salazar  <https://orcid.org/0000-0003-1742-9957>

William O F Carvalho  <https://orcid.org/0000-0001-6178-0061>

Cesar Lopez Mercado  <https://orcid.org/0000-0002-5083-7162>

N Nedev  <https://orcid.org/0000-0003-3391-010X>

Faustino Reyes Gómez  <https://orcid.org/0000-0001-5758-0489>

### References

- [1] Gao D and Zhou Z 2022 Silicon-based optoelectronics: progress towards large scale optoelectronic integration and applications *Front. Optoelectron.* **15** 2–3
- [2] Shi W H, Lv W M, Sun T Y and Zhang B S 2019 Optoelectronic platform and technology *Front. Inf Technol. Electron. Eng.* **20** 439–57
- [3] Băjenescu T M I 2021 Miniaturisation of electronic components and the problem of devices overheating *EEA -Electroteh. Electron. Autom.* **69** 53–58
- [4] Song H *et al* 2022 Highly-integrated, miniaturized, stretchable electronic systems based on stacked multilayer network materials *Sci. Adv.* **3785** 1–13
- [5] Meng Y, Liu A, Guo Z, Liu G, Shin B, Noh Y Y, Fortunato E, Martins R and Shan F 2018 Electronic devices based on oxide thin films fabricated by fiber-to-film process *ACS Appl. Mater. Interfaces* **10** 18057–65
- [6] Vyas S 2020 A short review on properties and applications of zinc oxide based thin films and devices: ZnO as a promising material for applications in electronics, optoelectronics, biomedical and sensors *Johns. Matthey Technol. Rev.* **64** 202–18
- [7] Gyanan M S and Kumar A 2016 Tunable dielectric properties of TiO<sub>2</sub> thin film based MOS systems for application in microelectronics *Superlattices Microstruct.* **100** 876–85
- [8] Jany R *et al* 2014 Monolithically integrated circuits from functional oxides *Adv. Mater. Interfaces* **1** 1–7
- [9] Liu A, Zhu H, Sun H, Xu Y and Noh Y Y 2018 Solution processed metal oxide high- $\kappa$  dielectrics for emerging transistors and circuits *Adv. Mater.* **30** 1–40
- [10] Palumbo F, Wen C, Lombardo S, Pazos S, Aguirre F, Eizenberg M, Hui F and Lanza M 2020 A review on dielectric breakdown in thin dielectrics: silicon dioxide, high- $\kappa$ , and layered dielectrics *Adv. Funct. Mater.* **30** 1–26
- [11] Li Q, Xiong H D, Liang X, Zhu X, Gu D, Ioannou D E, Baumgart H and Richter C A 2014 Self-assembled

- nanowire array capacitors: capacitance and interface state profile *Nanotechnology* **25** 1–7
- [12] Cetinkaya A O, Kaya S, Aktag A, Budak E and Yilmaz E 2015 Structural and electrical characterizations of BiFeO<sub>3</sub> capacitors deposited by sol-gel dip coating technique *Thin Solid Films* **590** 7–12
- [13] Xia P, Feng X, Ng R J, Wang S, Chi D, Li C, He Z, Liu X and Ang K W 2017 Impact and origin of interface states in MOS capacitor with monolayer MoS<sub>2</sub> and HfO<sub>2</sub> high-k dielectric *Sci. Rep.* **7** 1–9
- [14] Zhang X, Zhang S, Zhu H and Pan X 2018 Frequency dispersion analysis of thin dielectric MOS capacitor in a five-element model *J. Phys. D: Appl. Phys.* **51** 1–9
- [15] Wang C, Osada M, Ebina Y, Li B W, Akatsuka K, Fukuda K, Sugimoto W, Ma R and Sasaki T 2014 All-nanosheet ultrathin capacitors assembled layer-by-layer via solution-based processes *ACS Nano* **8** 2658–66
- [16] Khan M S, Kim H J, Kim Y H, Ebina Y, Sugimoto W, Sasaki T and Osada M 2020 Scalable design of two-dimensional oxide nanosheets for construction of ultrathin multilayer nanocapacitor *Small* **16** 1–6
- [17] Gaur A, Agarwal T, Asselberghs I, Iuliana Radu M H and L D 2017 A MOS capacitor model for ultra-thin 2D semiconductors: the impact of interface defects and channel resistance *2D Mater.* **7** 1–16
- [18] Li L, Zhang X, Chen H, Sun X, Yuan H and Xu H 2017 Modeling of structure effect for ferroelectric capacitor based on poly(vinylidene fluoride-trifluoroethylene) ultrathin films *Polymers* **10** 23–25
- [19] Xu K 2021 Silicon electro-optic micro-modulator fabricated in standard CMOS technology as components for all silicon monolithic integrated optoelectronic systems *J. Micromech. Microeng.* **31** 1–11
- [20] Wong H, Zhang J, Iwai H and Kakushima K 2021 Characteristic variabilities of subnanometer EOT La<sub>2</sub>O<sub>3</sub> gate dielectric film of nano CMOS devices *Nanomaterials* **11** 1–10
- [21] Li S, Ojima N, Xu Z and Iizuka T 2022 Analysis and simulation of MOSFET-based gate- voltage-independent capacitor *Jpn. J. Appl. Phys.* **61** 1–7
- [22] Liu L, Kawaharamura T, Sakamoto M, Nishi M, Dang G T and Sato S 2021 The quality improvement of yttrium oxide thin films grown at low temperature via the third-generation mist chemical vapor deposition using oxygen-supporting sources *Phys. Status Solidi b* **258** 1–8
- [23] Mahajan A M, Khairnar A G and Thibeault B J 2014 Electrical properties of MOS capacitors formed by PEALD grown Al<sub>2</sub>O<sub>3</sub> on silicon *Semiconductors* **48** 497–500
- [24] Jung H Y, Choi Y Y, Kim H K and Choi D J 2012 Deposition temperature effect of the memory characteristics for Al<sub>2</sub>O<sub>3</sub>/Y<sub>2</sub>O<sub>3</sub>/SiO<sub>2</sub> (AYO) multi-stacked film *J. Ceram. Soc. Jpn.* **120** 525–9
- [25] Leskelä M, Mattinen M and Ritala M 2019 Review article: atomic layer deposition of optoelectronic materials *J. Vac. Sci. Tech. B* **37** 1–24
- [26] Nguyen H M T, Tang H Y, Huang W F and Lin M C 2014 Mechanisms for reactions of trimethylaluminum with molecular oxygen and water *Comput. Theor. Chem.* **1035** 39–43
- [27] Cho G Y, Noh S, Lee Y H, Ji S and Cha S W 2014 Study of Y<sub>2</sub>O<sub>3</sub> thin film prepared by plasma enhanced atomic layer deposition *ECS Trans.* **64** 15–21
- [28] López J, Solorio E, Borbon-Núñez H A, Castillon F F, Machorro R, Nedev N, Farias M H and Tiznado H 2017 Refractive index and bandgap variation in Al<sub>2</sub>O<sub>3</sub>-ZnO ultrathin multilayers prepared by atomic layer deposition *J. Alloys Compd.* **691** 308–15
- [29] López J, Martínez J, Abundiz N, Domínguez D, Murillo E, Castillón F F, MacHorro R, Farias M H and Tiznado H 2016 Thickness effect on the optical and morphological properties in Al<sub>2</sub>O<sub>3</sub>/ZnO nanolaminate thin films prepared by atomic layer deposition *Superlattices Microstruct.* **90** 265–73
- [30] Park I S, Chan Jung Y, Seong S, Ahn J, Kang J, Noh W and Lansalot-Matras C 2014 Atomic layer deposition of Y<sub>2</sub>O<sub>3</sub> films using heteroleptic liquid (iPrCp)<sub>2</sub>Y(iPr-amd) precursor *J. Mater. Chem.* **2** 9240–7
- [31] Xiang Y, Zhou C, Jia E and Wang W 2015 Oxidation precursor dependence of atomic layer deposited Al<sub>2</sub>O<sub>3</sub> films in a-Si:H(i)/Al<sub>2</sub>O<sub>3</sub> surface passivation stacks *Nanoscale Res. Lett.* **10** 9–11
- [32] Jakschik S, Schroeder U, Hecht T, Krueger D, Dollinger G, Bergmaier A, Luhmann C and Bartha J W 2003 Physical characterization of thin ALD-Al<sub>2</sub>O<sub>3</sub> films *Appl. Surf. Sci.* **211** 352–9
- [33] Mai L, Boysen N, Subaşı E, De Los Arcos T, Rogalla D, Grundmeier G, Bock C, Lu H L and Devi A 2018 Water assisted atomic layer deposition of yttrium oxide using tris(N,N0-diisopropyl-2-dimethylamido-guanidinato) yttrium(III): process development, film characterization and functional properties† *RSC Adv.* **8** 4987–94
- [34] Nicollian E H and B J R 1982 *MOS (Metal Oxide Semiconductor) Physics and Technology* vol 74 (A Wiley—Interscience publication) pp 1–644
- [35] Sze S M and N K K 2006 *Physics of Semiconductor Devices* Ed John Wiley and Sons (Wiley-Interscience) p 431–510
- [36] Woollam J A 2011 *CompleteEASE™ Data Analysis Manual* 1st edn ed J A Woollam Co pp 1–186
- [37] Irene H G T and A E 2005 JEMS: a journal of emergency medical services *Handbook of Ellipsometry* (William Andrew, Inc.) vol 30 pp 3–298
- [38] Fujiwara H 2007 *Spectroscopic Ellipsometry: Principles and Applications* (Wiley) pp 1–11
- [39] Niinistö J, Putkonen M and Niinistö L 2004 Processing of Y<sub>2</sub>O<sub>3</sub> thin films by atomic layer deposition from cyclopentadienyl-type compounds and water as precursors *Chem. Mater.* **16** 2953–8
- [40] Niinistö J, Putkonen M, Niinistö L, Stoll S L, Kukli K, Sajavaara T, Ritala M and Leskela M 2005 Controlled growth of HfO<sub>2</sub> thin films by atomic layer deposition from cyclopentadienyl-type precursor and water *J. Mater. Chem.* **15** 2271–5
- [41] Niinistö J, Rahtu A, Putkonen M, Ritala M, Leskelä M and Niinistö L 2005 In situ quadrupole mass spectrometry study of atomic-layer deposition of ZrO<sub>2</sub> using Cp<sub>2</sub>Zr(CH<sub>3</sub>)<sub>2</sub> and water *Langmuir* **21** 7321–5
- [42] Gaboriaud R J, Paumier F and Lacroix B 2016 Disorder-order phase transformation in a fluorite-related oxide thin film: in-situ x-ray diffraction and modelling of the residual stress effects *Thin Solid Films* **601** 84–88
- [43] Novita M, Wibowo S, Nada N Q and Ogasawara K 2019 Comparative study on r-line and u-band energies of ruby estimated from one-electron and many-electron first-principles approaches *J. Phys.: Conf. Ser.* **1179** 2–5
- [44] Getz M N, Povoli M and Monakhov E 2022 Improving ALD-Al<sub>2</sub>O<sub>3</sub> surface passivation of Si utilizing pre-existing SiO<sub>x</sub> *IEEE J. Photovolt.* **12** 929–36
- [45] Freeze C R, Stemmer S, Freeze C R and Stemmer S 2016 Role of film stoichiometry and interface quality in the performance of (Ba, Sr) TiO<sub>3</sub> tunable capacitors with high figures of merit *Appl. Phys. Lett.* **109** 192904
- [46] Yang W S, Yeom S J, Kim N K, Kweon S Y and Roh J S 2000 Effects of crystallization annealing sequence for SrBi<sub>2</sub>Ta<sub>2</sub>O<sub>9</sub> (SBT) film on Pt/SBT interface morphology

- and electrical properties of ferroelectric capacitor *Jpn. J. Appl. Phys.* **39** 5465–8
- [47] Wenger C *et al* 2006 High-quality  $\text{Al}_2\text{O}_3/\text{Pr}_2\text{O}_3/\text{Al}_2\text{O}_3$  MIM capacitors for RF applications *IEEE Trans. Electron Devices* **53** 1937–9
- [48] Kotru S, Batra V and Harshan V N 2018 Electrical behavior of  $\text{Pb}_{0.95}\text{La}_{0.05}\text{Zr}_{0.54}\text{Ti}_{0.46}\text{O}_3$  thin film based capacitors: influence of space charge region *J. Appl. Phys.* **124** 1–9
- [49] Mahat A M, Mastuli M S, Badar N and Kamarulzaman N 2021 Novel  $\text{Al}_{1.997}\text{Hf}_{0.003}\text{O}_3$  high-k gate dielectric thin films grown by pulsed laser deposition using pre-synthesized target material *J. Mater. Sci.: Mater. Electron.* **32** 10927–42
- [50] Illarionov Y Y *et al* 2019 Ultrathin calcium fluoride insulators for two-dimensional field-effect transistors *Nat. Electron.* **2** 230–5
- [51] He Y *et al* 2021 Robust nanocapacitors based on wafer-scale single-crystal hexagonal boron nitride monolayer films *ACS Appl. Nano Mater.* **4** 5685–95
- [52] Kaisti M 2017 Detection principles of biological and chemical FET sensors *Biosens. Bioelectron.* **98** 437–48